Phase Equilibria in the Fe-Mo-Nb System at 1100 °C and 1200 °C

LEI ZOU, ZETING DU, CUIPING GUO, CHANGRONG LI, and ZHENMIN DU

The isothermal sections of the Fe-Mo-Nb system at 1100 °C and 1200 °C were constructed using X-ray diffraction and scanning electron microscopy coupled with energy dispersive spectroscopy. The experimental results indicate that the isothermal section at 1100 °C consists of six single-phase, nine two-phase, and four three-phase regions. At 1200 °C, there are six single-phase, eight two-phase, and three three-phase regions. The maximum solubilities of Mo in C14-Fe_2Nb and μ-Fe_7Nb_6, and Nb in μ-Fe_7Mo_6 were determined to be about 26.97, 7.35, 19.74 at. pct at 1100 °C, respectively. The corresponding maximum solubilities of Mo at 1200 °C were determined to be about 25.08, 10.40, 23.85 at. pct at 1200 °C, respectively. No ternary compounds were observed at 1100 °C and 1200 °C.

https://doi.org/10.1007/s11661-018-4962-z

I. INTRODUCTION

NEXT-GENERATION high-performance steel is required for lightweight design and advanced energy applications.[1] In general, an increase in strength is accompanied by a decrease in toughness and plasticity, which results in stress-induced cracking and difficulty in forming.[2] Therefore, current research focused on improving the strength of steel while simultaneously increasing toughness.

The addition of Mo and Nb can effectively improve the strength of steel due to solution, fine grain, and dispersion strengthening effects. The formation of fine precipitates of C14-Fe_2Nb offer considerable strength improvement and creep resistance.[3–5] Mo and Nb have strong carbide-forming ability in steel and carbides of type MC and M_2C can prevent austenite grain growth during austenization which can improve the fracture toughness of tempered martensite.[6–8] However, the addition of high concentrations of Mo increases the probability of formation of the σ phase which is extremely brittle and deteriorates the toughness of the steel.[9–11] Thus, it is important to obtain the relevant phase equilibria information of the Fe-Mo-Nb ternary system for the development and design of ultrastrong steel.

LEI ZOU, ZETING DU, CUIPING GUO, CHANGRONG LI, and ZHENMIN DU are with the School of Materials Science and Engineering, University of Science and Technology Beijing, Beijing 100083, P.R. China. Contact e-mails: duzm@ustb.edu.cn, cpguo2003@sina.com
Manuscript submitted April 10, 2018.
Article published online October 25, 2018

II. LITERATURE INFORMATION

A. *Fe-Mo System*

The Fe-Mo system was first investigated by Sykes.[12] Subsequently, the Fe-Mo phase diagram has been experimentally revised by many researchers.[13–22] Some reliable experimental data on the Fe-Mo system were compiled by Guillermet.[23] Then, Gustafson[24] revised compositions of the R and σ phases using electron-probe microanalysis. Rajkumar and Kumar[25] performed a thermodynamic assessment of the Fe-Mo system based on reliable experimental data. In the present work, the Fe-Mo phase diagram assessed by Rajkumar and Kumar[25] is adopted.

B. *Fe-Nb System*

The phase equilibria of the Fe-Nb system were first determined by Voronov.[26] The results of various investigations[15,26–35] have been subsequently found to agree well in the Fe-rich portions of the Fe-Nb phase diagram. Recently, a comprehensive Fe-Nb phase diagram was determined by Voß *et al.*[36] Based on the experimental results mentioned above, Jacob *et al.*[37] assessed the Fe-Nb phase diagram, and it is the results of this work that are used in this paper.

C. *Mo-Nb System*

The Mo-Nb phase diagram was first constructed by Rudy *et al.*[38] using the Pirani method. Reliable experimental data on the Mo–Nb system were measured by Kocherzhinskii and Vasilenko[39] using high-temperature differential thermal analysis. The Mo–Nb phase diagram assessed by Xiong *et al.*[40] was in reasonable

agreement with the experimental data of Reference 39. Therefore, the Mo–Nb phase diagram using the thermodynamic parameters of Reference 40 is adopted in the current work.

The phase diagrams adopted in this study for the three binary systems Fe-Mo,[25] Fe-Nb,[37] and Mo-Nb[40] are shown in Figure 1 and crystallographic data are also listed in Table I.[16,29,38]

D. *Fe-Mo-Nb System*

The isothermal section of the Fe-Mo-Nb system at 900 °C was measured by Smirnova *et al.*[41] and is also

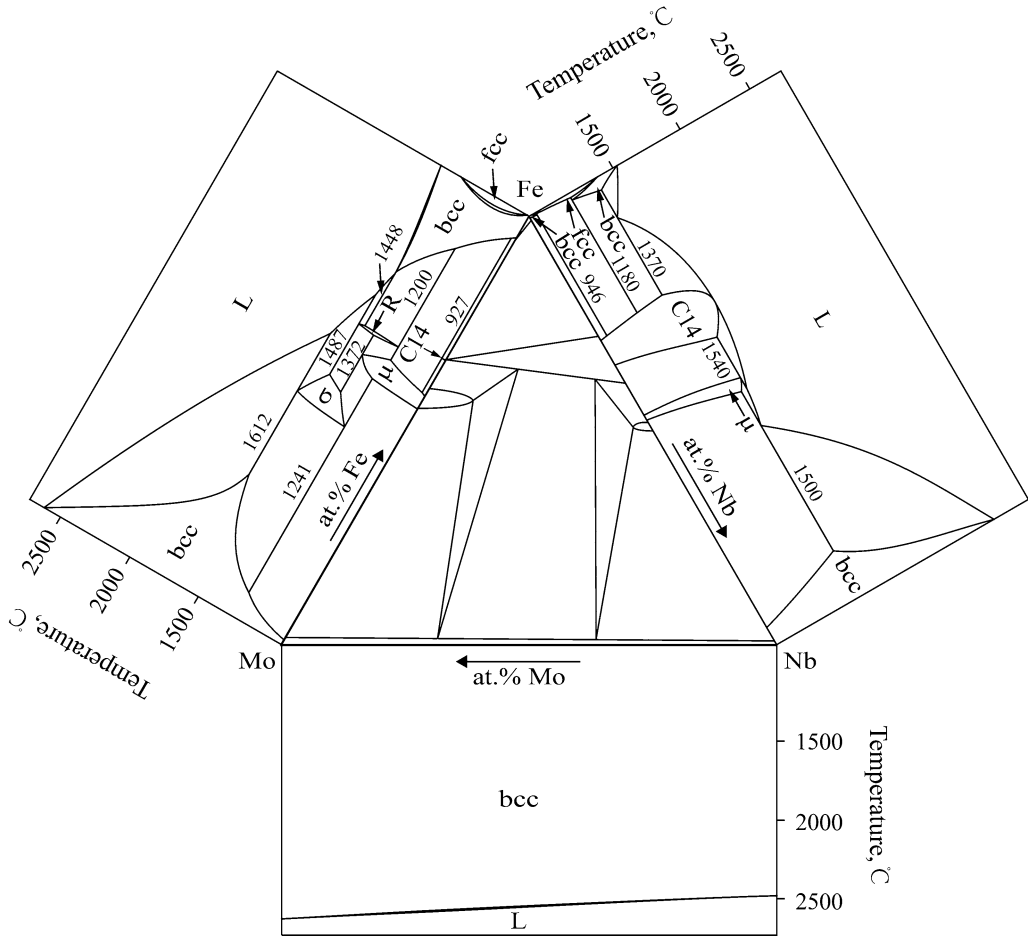

Fig. 1—Compilation of the calculated Fe-Mo, Fe-Nb, and Mo-Nb phase diagrams using the thermodynamic parameters of Refs. [25, 37, 40] and the constructed isothermal section of the Fe-Mo-Nb system at 900 °C based on the experimental data of Ref. [41].

Table I. Crystallographic Data of the Phases in the Fe-Mo-Nb System

System	Phase	Struktur-bericht	Prototype	Pearson Symbol	Space Group	Ref.
Fe-Mo	fcc	A1	Cu	cF4	$Fm\bar{3}m$	16
	bcc	A2	W	cI2	$Im\bar{3}m$	16
	C14-Fe_2Mo	C14	$MgZn_2$	hP12	$P6_3/mmc$	16
	R		R-(Co,Cr,Mo)	hR53	$R\bar{3}$	16
	μ-Fe_7Mo_6	$D8_5$	Fe_7W_6	hR13	$R\bar{3}m$	16
	σ	$D8_b$	σ-CrFe	tP30	$P42/mnm$	16
Fe-Nb	fcc	A1	Cu	cF4	$Fm\bar{3}m$	29
	bcc	A2	W	cI2	$Im\bar{3}m$	29
	μ-Fe_7Nb_6	$D8_5$	Fe_7W_6	hR13	$R\bar{3}m$	29
	C14-Fe_2Nb	C14	$MgZn_2$	hP12	$P6_3/mmc$	29
Mo-Nb	bcc	A2	W	cI2	$Im\bar{3}m$	38

shown in Figure 1. Harikumar and Raghavan[42] have also presented the Fe-rich (95 at. pct Fe) corners of the isothermal sections of the Fe-Mo-Nb system at 1000 °C, 1050 °C, 1150 °C, and 1250 °C. Villars *et al.*[43] have given summary of the Fe-Mo-Nb system based on the information presented in References 41 and 42.

III. EXPERIMENTAL PROCEDURES

High-purity starting materials were used to prepare the ternary alloys in the form of Fe bulk (99.99 wt pct), Mo rods (99.99 wt pct), and Nb rods (99.99 wt pct). All samples (with total masses of 5 g) were prepared by arc-melting them on a water-cooled copper crucible under an argon atmosphere of high purity.

The arc furnace chamber was first evacuated and flushed with high-purity Ar at least four times. Then, a piece of pure Ti was re-melted at least three times before alloying in order to consume any residual oxygen. All samples were inverted and re-melted at least five times to ensure compositional homogeneity. Then, the ingots were weighed and the alloys whose burning losses did not exceed 0.5 wt pct were chosen to the experiments. (Unused samples could be re-fabricated if required.) Samples were cut from each of the alloy ingots and encapsulated in quartz tubes under vacuum.

In Reference 41, the Fe-Mo-Nb ternary alloy samples were heat treated at 900 °C for 100 days before constructing the isothermal section. Considering that higher diffusion rates occur at 1100 °C and 1200 °C, 30-day heat treatment was initially used in the experiments. However, some samples did not reach equilibrium condition. During further experimentation, it was found that the samples essentially reached equilibrium condition after 60 (1100 °C) and 45 (1200 °C) days of heat treatment. Therefore, these heating regimes were adopted in the present work. In order to further confirm the equilibrium microstructure, however, an extra period of 30-day heat treatment (at 1100 °C) was used for alloys #14 and #18. Ultimately, the sample capsules were quenched in cold water to preserve the high-temperature phase equilibria.

The annealed samples were divided into two parts. One part was prepared for X-ray diffraction (XRD) analysis, the other for metallographic analysis using scanning electron microscopy (SEM). The compositions of the alloys were measured in area mode employing the entire sample under low magnification. For large phase areas, the composition was measured three times in area mode using a square and the final results obtained by averaging the measurements. For small phase areas, the composition was measured five times in point mode at high magnification and the measurements were averaged to yield the final results.

The observation of equilibrium phases and compositional analyses were carried out using a commercially available SEM (LEO-1450, Zeiss, Germany) coupled with an energy dispersive spectrometer (NORAN-7 Thermo Scientific, USA). An acceleration voltage of 20 kV was employed. Composition measurements were conducted at least three times. The X-ray diffraction measurements were carried out on bulk samples using a diffractometer (SmartLab, Rigaku, Japan) employing Cu-Kα radiation (λ = 1.5406 Å) at 40 kV and 150 mA. Diffraction spectra were collected between 20 and 100 deg with a scan step size of 0.02 deg.

IV. RESULTS AND DISCUSSION

A. *Isothermal Section at 1100 °C*

To investigate the isothermal section of the Fe-Mo-Nb system at 1100 °C, 21 alloy samples were heat treated at 1100 °C for 60 days or longer (*i.e.*, alloys #14 and #18 which were heated for extra 30 days). The experimental results indicated that there were no obvious differences between the microstructures of the alloys annealed for 90 days compared to those annealed for 60 days. The compositions of alloys and constituent phases determined by EDS measurement are summarized in Table II. The measured compositions of the alloys are in good agreement with their nominal compositions (the slight deviations between the measured compositions of alloys and the tie lines are related to the errors involved the EDS measurement).

Figure 2 shows the XRD pattern and backscattered electron (BSE) micrograph of alloy #3. The XRD pattern shown in Figure 2(a) only contains diffraction peaks corresponding to the bcc(Fe) and C14-Fe_2Nb. Moreover, it is clear that a gray phase is in equilibrium with a dark phase from Figure 2(b). The compositions of the gray and dark phases were determined to be 72.34Fe-3.08Mo-24.58Nb and 97.21Fe-1.61Mo-1.18Nb, respectively (in terms of at. pct, as will be similarly used hereinafter). A small amount of a dark gray phase can also be vaguely observed in the BSE micrograph; however, the composition of this phase is almost the same as that of the gray phase according to the EDS results. At the same time, some black spots can be observed in Figure 2(b), but these are merely pores caused by the metallographic preparation process. Overall, the XRD and EDS analyses indicate that the gray phase is C14-Fe_2Nb, and the dark phase is bcc(Fe).

In the Fe-rich corner, there are two-phase regions fcc(Fe) + bcc(Fe) and fcc(Fe) + C14-Fe_2Nb in the Fe-Mo[25] and Fe-Nb[37] phase diagrams at 1100 °C, respectively. Therefore, there should be a three-phase region fcc(Fe) + bcc(Fe) + C14-Fe_2Nb in the isothermal section of the Fe-Mo-Nb system at 1100 °C, which we illustrate in the present work using dotted lines.

Figure 3 shows the XRD patterns and BSE micrographs of alloys #6 and #7. Diffraction peaks corresponding to the bcc(Fe) and μ-Fe_7Mo_6 clearly occur in Figures 3(a) and (c). In addition, the XRD pattern of alloy# 6 shown in Figure 3(a) contained the diffraction peaks corresponding to C14-Fe_2Nb. Correspondingly, a microstructure revealing an equilibrium involving three-phase can be observed in Figure 3(b). The EDS measurements determined the compositions of these phases to be 88.29Fe-11.02Mo-0.69Nb (dark phase), 65.47Fe-27.61Mo-6.92Nb (dark gray phase), and 60.93Fe-35.12Mo-3.95Nb (gray phase). Therefore, the

Table II. Summary of Experimental Results of the Fe-Mo-Nb Alloys Annealed at 1100 °C

	Measured Composition, Atomic Percent				Phase Composition, Atomic Percent		
No.	Fe	Mo	Nb	Equilibrium Phase	Fe	Mo	Nb
#1	95.71	3.44	0.85	bcc(Fe)	96.25	2.91	0.84
#2	78.41	12.65	8.94	bcc(Fe)	93.07	5.91	1.02
				C14-Fe_2Nb	67.56	17.12	15.32
#3	75.34	2.84	21.82	bcc(Fe)	97.21	1.61	1.18
				C14-Fe_2Nb	72.34	3.08	24.58
#4	72.25	20.73	7.02	bcc(Fe)	91.26	7.91	0.83
				C14-Fe_2Nb	66.39	24.99	8.62
#5	71.46	24.16	4.38	bcc(Fe)	90.39	8.84	0.77
				C14-Fe_2Nb	66.71	26.33	6.96
				μ-Fe_7Mo_6	59.95	34.93	5.12
#6	69.66	25.79	4.55	bcc(Fe)	90.18	9.33	0.49
				C14-Fe_2Nb	65.47	27.61	6.92
				μ-Fe_7Mo_6	60.53	35.52	3.95
#7	66.25	31.76	1.99	bcc(Fe)	89.58	10.13	0.29
				μ-Fe_7Mo_6	60.56	36.58	2.86
#8	66.10	7.18	26.72	C14-Fe_2Nb	65.65	7.48	26.87
#9	63.54	21.86	14.60	C14-Fe_2Nb	65.78	19.59	14.63
				μ-Fe_7Mo_6	58.33	27.78	13.89
#10	63.31	17.47	19.22	C14-Fe_2Nb	65.62	14.60	19.78
				μ-Fe_7Mo_6	57.25	26.37	16.38
#11	63.25	29.48	7.27	C14-Fe_2Nb	66.41	25.06	8.53
				μ-Fe_7Mo_6	59.62	33.53	6.85
#12	60.42	6.22	33.36	C14-Fe_2Nb	64.11	5.04	30.85
				μ-Fe_7Nb_6	49.89	7.73	42.38
				bcc(Mo,Nb)	5.78	46.76	47.46
#13	57.19	36.09	6.72	μ-Fe_7Mo_6	56.51	36.69	6.80
#14	56.63	21.62	21.75	C14-Fe_2Nb	64.79	11.38	23.83
				μ-Fe_7Mo_6	55.41	24.85	19.74
				bcc(Mo,Nb)	6.43	65.75	27.82
#15	56.50	3.11	40.39	C14-Fe_2Nb	65.31	1.92	32.77
				μ-Fe_7Nb_6	52.51	2.93	44.56
#16	51.81	10.38	37.81	C14-Fe_2Nb	65.68	4.55	29.77
				μ-Fe_7Nb_6	51.76	6.99	41.25
				bcc(Mo,Nb)	6.84	44.39	48.77
#17	42.60	44.98	12.42	μ-Fe_7Mo_6	54.79	33.62	11.59
				bcc(Mo,Nb)	6.56	77.73	15.71
#18	32.43	35.10	32.47	C14-Fe_2Nb	64.81	9.66	25.53
				bcc(Mo,Nb)	6.11	57.21	36.68
#19	24.84	54.04	21.12	μ-Fe_7Mo_6	54.83	29.16	16.01
				bcc(Mo,Nb)	6.55	70.53	22.92
#20	13.75	18.96	67.29	μ-Fe_7Nb_6	49.34	4.07	46.59
				bcc(Mo,Nb)	4.45	23.64	71.91
#21	13.93	6.28	79.79	μ-Fe_7Nb_6	50.15	2.48	47.37
				bcc(Mo,Nb)	3.83	6.49	89.68

dark, dark gray, and gray phases correspond to bcc(Fe), C14-Fe_2Nb, and μ-Fe_7Mo_6, respectively. Similar results were observed for alloy #5. The maximum solubility of Mo in C14-Fe_2Nb was determined to be about 26.97 at. pct at 1100 °C, which is the average composition of Mo in C14-Fe_2Nb in alloys #5 and #6 as measured by EDS.

A two-phase microstructure is clearly apparent in Figure 3(d). EDS measurement determined the compositions of these phases to be 87.89Fe-11.92Mo-0.19Nb (dark phase) and 61.56Fe-35.58Mo-2.86Nb (gray phase). Hence, alloy #7 is located in the bcc(Fe) + μ-Fe_7Mo_6 two-phase region, in agreement with the XRD pattern shown in Figure 3(c).

The results obtained for alloys #12 are shown in Figure 4 which reveal a three-phase microstructure. In Figure 4(b), the compositions of the phases indicated correspond to 65.68Fe-5.94Mo-28.38Nb (dark gray phase), 49.89Fe-7.73Mo-42.38Nb (gray phase), and 5.78Fe-46.76Mo-47.46Nb (bright phase). Combining the results obtained using XRD and EDS, it can be concluded that alloy #12 is located in the C14-Fe_2Nb + μ-Fe_7Nb_6 + bcc(Mo, Nb) three-phase region. The EDS

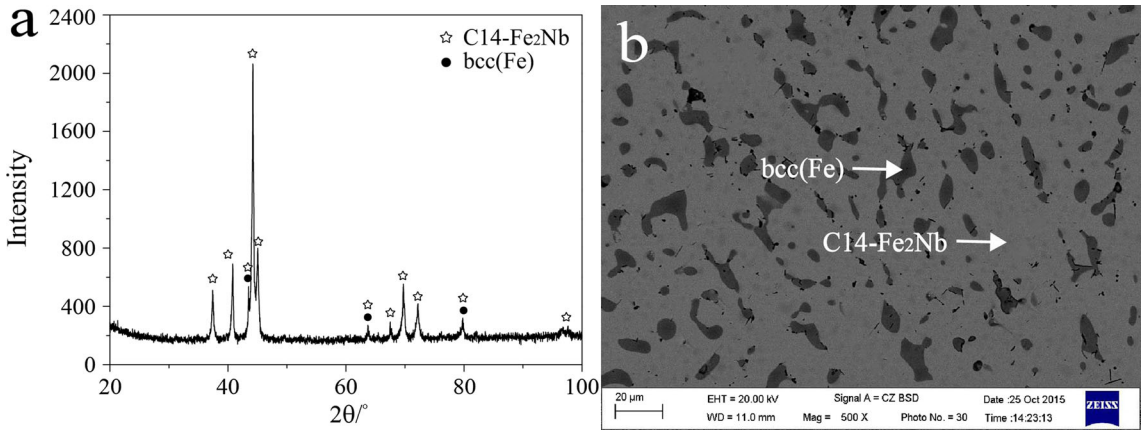

Fig. 2—Alloy #3 annealed at 1100 °C: (*a*) XRD pattern, (*b*) BSE micrograph.

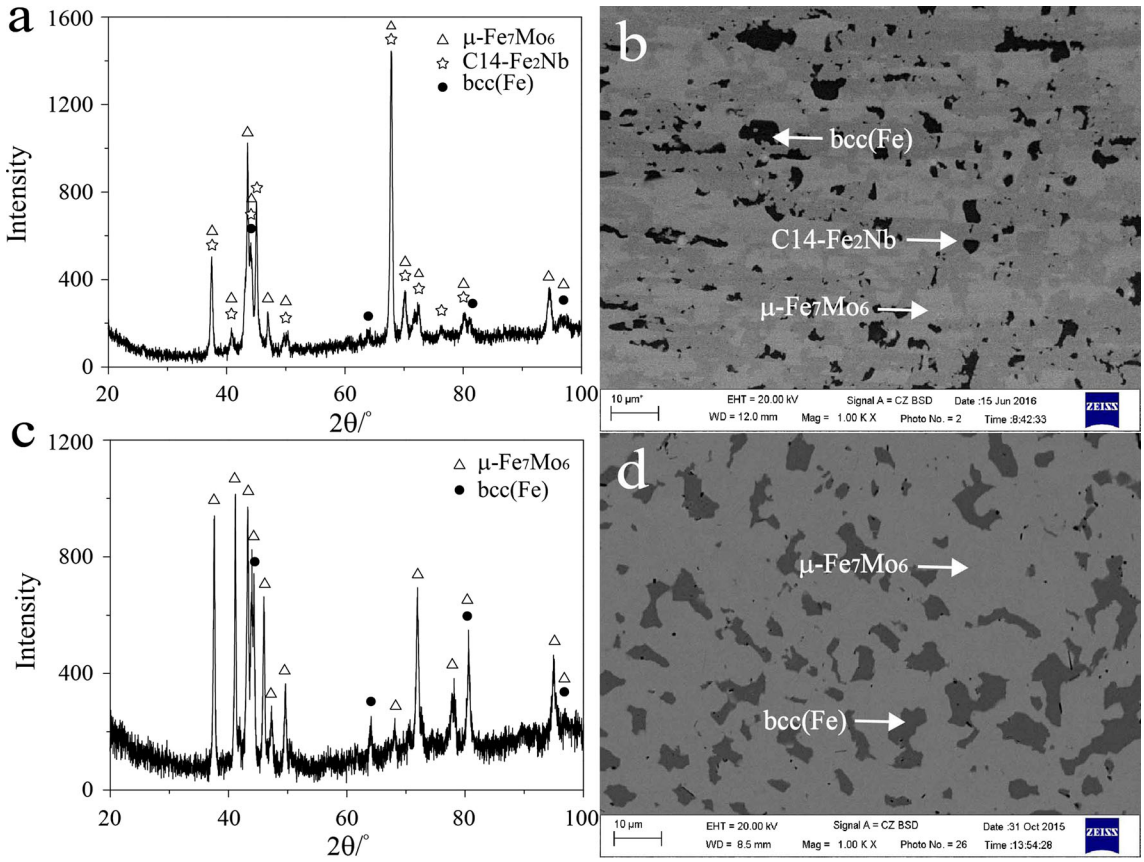

Fig. 3—Alloy annealed at 1100 °C: (*a*) XRD pattern of #6, (*b*) BSE micrograph of #6, (*c*) XRD pattern of #7, (*d*) BSE micrograph of #7.

analysis further shows that the maximum solubility of Mo in μ-Fe_7Nb_6 is about 7.35 at. pct at this temperature (1100 °C).

Figure 5 shows two XRD patterns and two BSE micrographs of alloy #14 obtained under different conditions. Figures 5(a) and (b) were recorded using the as-cast alloy, and Figures 5(c) and (d) using the sample annealed for 90 days.

In Figure 5(b), the bright primary solidification phase was determined to be μ-Fe_7Mo_6 (53.05Fe-28.84Mo-18.11Nb), and the lamellar microstructure was eutectic microstructure of μ-Fe_7Mo_6 + C14-Fe_2Nb. After annealing, a small amount of a white phase corresponding to bcc(Mo, Nb) (6.39Fe-67.79Mo-25.82Nb) is observed to have precipitated, as shown in Figure 5(d). The typical eutectic microstructure corresponding to μ-Fe_7Mo_6 +

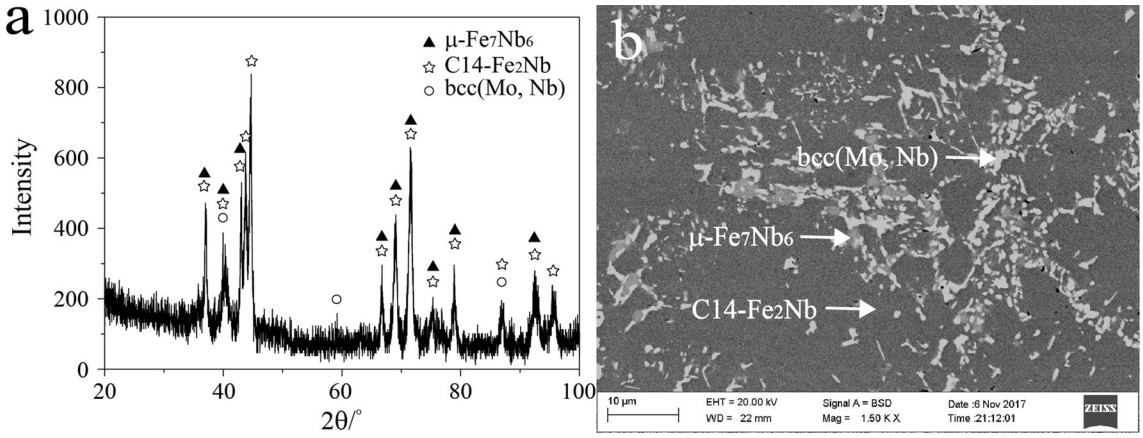

Fig. 4—Alloy #12 annealed at 1100 °C: (*a*) XRD pattern, (*b*) BSE micrograph.

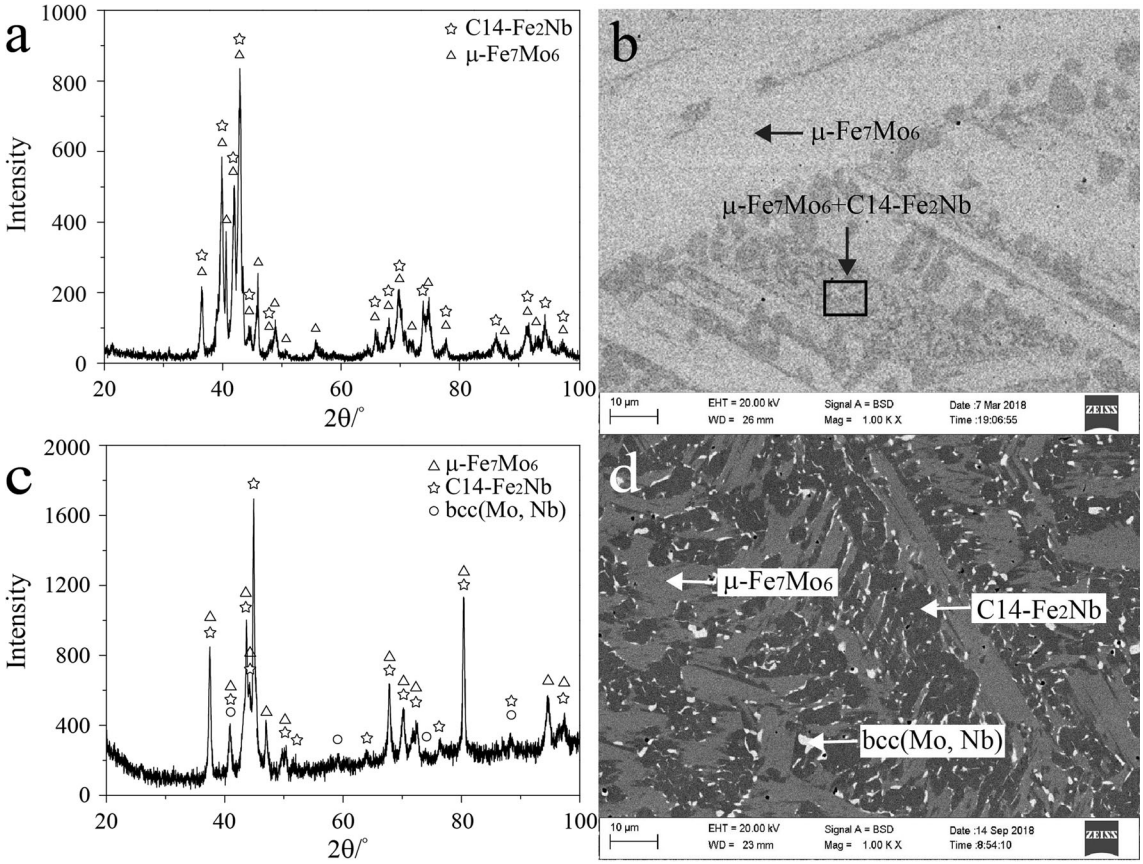

Fig. 5—As-cast alloy #14: (*a*) XRD pattern, (*b*) BSE micrograph, alloy #14 annealed at 1100 °C: (*c*) XRD pattern, (*d*) BSE micrograph.

C14-Fe_2Nb had disappeared. Thus, the annealed sample of alloy #14 can be considered to have reached equilibrium condition. Furthermore, according to the EDS analysis, the maximum solubility of Nb in μ-Fe_7Mo_6 is about 19.74 at. pct at 1100 °C.

The results obtained for alloys #17 and #20 are shown in Figure 6 which reveal them to have typical two-phase microstructures. The phases present in alloy #17 correspond to: 54.79Fe-33.62Mo-11.59Nb (gray phase), and 6.56Fe-77.73Mo-15.71Nb (bright phase) corresponding to μ-Fe_7Mo_6 and bcc(Mo, Nb), respectively. The phases present in alloy #20 correspond to: 49.34Fe-4.07Mo-46.59Nb (gray phase), and 4.45Fe-23.64Mo-71.91Nb (bright phase) corresponding to μ-Fe_7Nb_6 and bcc(Mo, Nb), respectively. The results are in agreement with the XRD patterns shown in Figures 6(a) and (c).

Figures 7(a) and (b) show the results for the as-cast alloy #18. Figure 7(b) shows that the as-cast sample only contains the primary solidification phase bcc(Mo, Nb) (8.13Fe-54.85Mo-37.02Nb) and gray phase

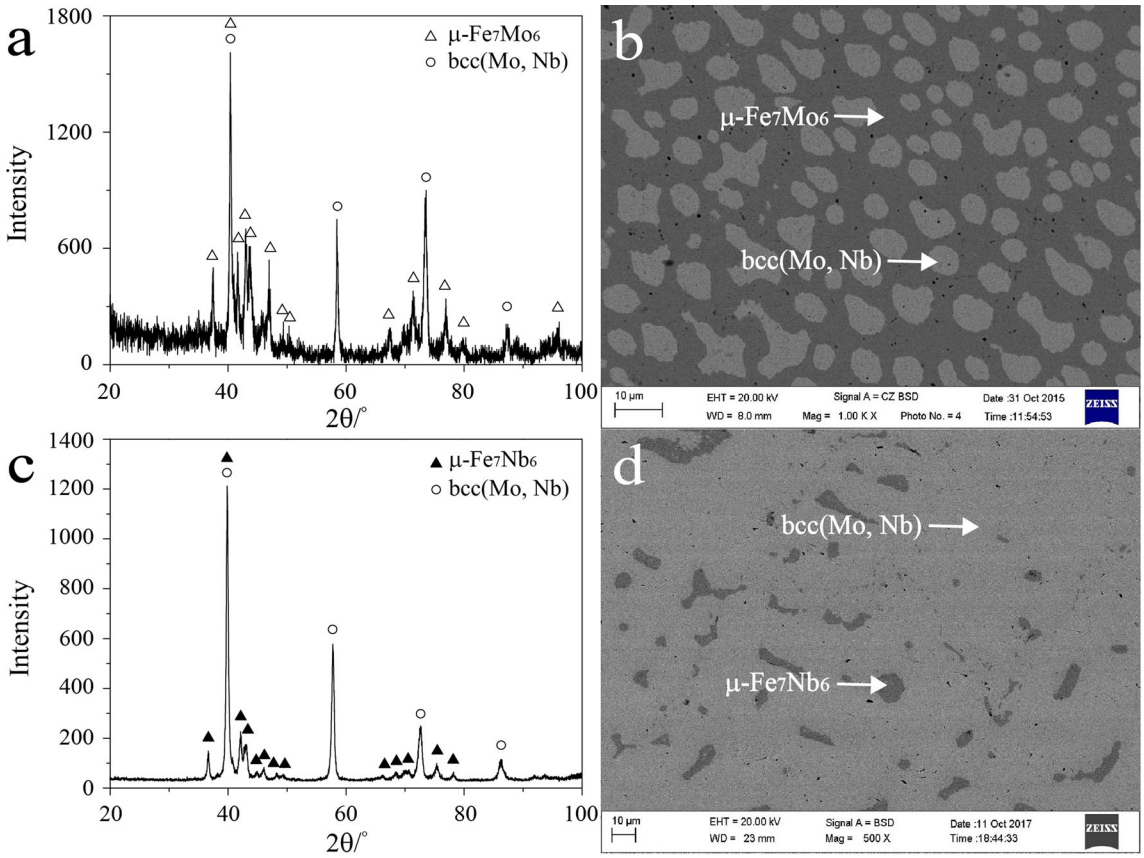

Fig. 6—Alloy annealed at 1100 °C: (*a*) XRD pattern of #17, (*b*) BSE micrograph of #17, (*c*) XRD pattern of #20, (*d*) BSE micrograph of #20.

μ-Fe_7Nb_6 (50.97Fe-18.61Mo-30.42Nb). The corresponding results for alloy #18 after annealing for 90 days are shown in Figures 7(c) and (d). A large amount of (dotted white) bcc(Mo, Nb) phase can be seen to have precipitated from the as-cast μ-Fe_7Nb_6 phase after annealing. The original μ-Fe_7Nb_6 phase has been transformed into C14-Fe_2Nb (63.81Fe-10.68Mo-25.51Nb). Thus, the annealed alloy #18 can be considered to have reached equilibrium condition. Also, alloy #18 can be seen to be located in the C14-Fe_2Nb + bcc(Mo, Nb) two-phase region.

Based on the experimental results presented above, the isothermal section of the Fe-Mo-Nb system at 1100 °C can be established, as presented in Figure 8. There are six single-phase regions: fcc(Fe), bcc(Fe), bcc(Mo, Nb), C14-Fe_2Nb, μ-Fe_7Mo_6, and μ-Fe_7Nb_6, and four three-phase regions: fcc(Fe) + bcc(Fe) + C14-Fe_2Nb, bcc(Fe) + C14-Fe_2Nb + μ-Fe_7Mo_6, C14-Fe_2Nb + μ-Fe_7Mo_6 + bcc(Mo, Nb), and C14-Fe_2Nb + μ-Fe_7Nb_6 + bcc(Mo, Nb) in this isothermal section. The solubilities of the C14-Fe_2Nb, μ-Fe_7Mo_6 and μ-Fe_7Nb_6 were determined at 1100 °C.

B. *Isothermal Section at 1200 °C*

To investigate the isothermal section of the Fe-Mo-Nb system at 1200 °C, 20 alloys were annealed at 1200 °C for 45 days. The results of the EDS analysis are given in Table III. As before, the error associated with EDS can lead to a slight deviation between the measured compositions of alloys and the tie lines.

Figure 9 shows the XRD pattern and BSE micrograph of alloy #7. In Figure 9(a), it can be seen that there are three groups of diffraction peaks associated with the bcc(Fe), C14-Fe_2Nb, and μ-Fe_7Mo_6 present in this alloy. The EDS analysis of alloy #7 reveals a typical three-phase microstructure bcc(Fe) + C14-Fe_2Nb + μ-Fe_7Mo_6 in agreement with the XRD pattern. Similar results were observed from alloy #6. According to the EDS analysis of alloys 6# and 7#, the maximum solubility of Mo in C14-Fe_2Nb is about 25.08 at. pct at 1200 °C.

The results obtained for alloy #14 at 1200 °C are shown in Figure 10. The XRD results indicate that C14-Fe_2Nb, μ-Fe_7Mo_6, and bcc(Mo, Nb) exist in this alloy. The BSE micrograph of the alloy confirms that a three-phase microstructure occurs, C14-Fe_2Nb + μ-Fe_7Mo_6 + bcc(Mo, Nb). Therefore, the C14-Fe_2Nb + μ-Fe_7Mo_6 + bcc(Mo, Nb) three-phase region can be constructed. The maximum solubility of Nb in μ-Fe_7Mo_6 was determined to be about 23.85 at. pct at 1200 °C.

The results obtained for alloy #16 are shown in Figure 11. In Figure 11(a), the XRD pattern includes the diffraction peaks corresponding to C14-Fe_2Nb, μ-Fe_7Nb_6, and bcc(Mo, Nb). In the BSE micrograph,

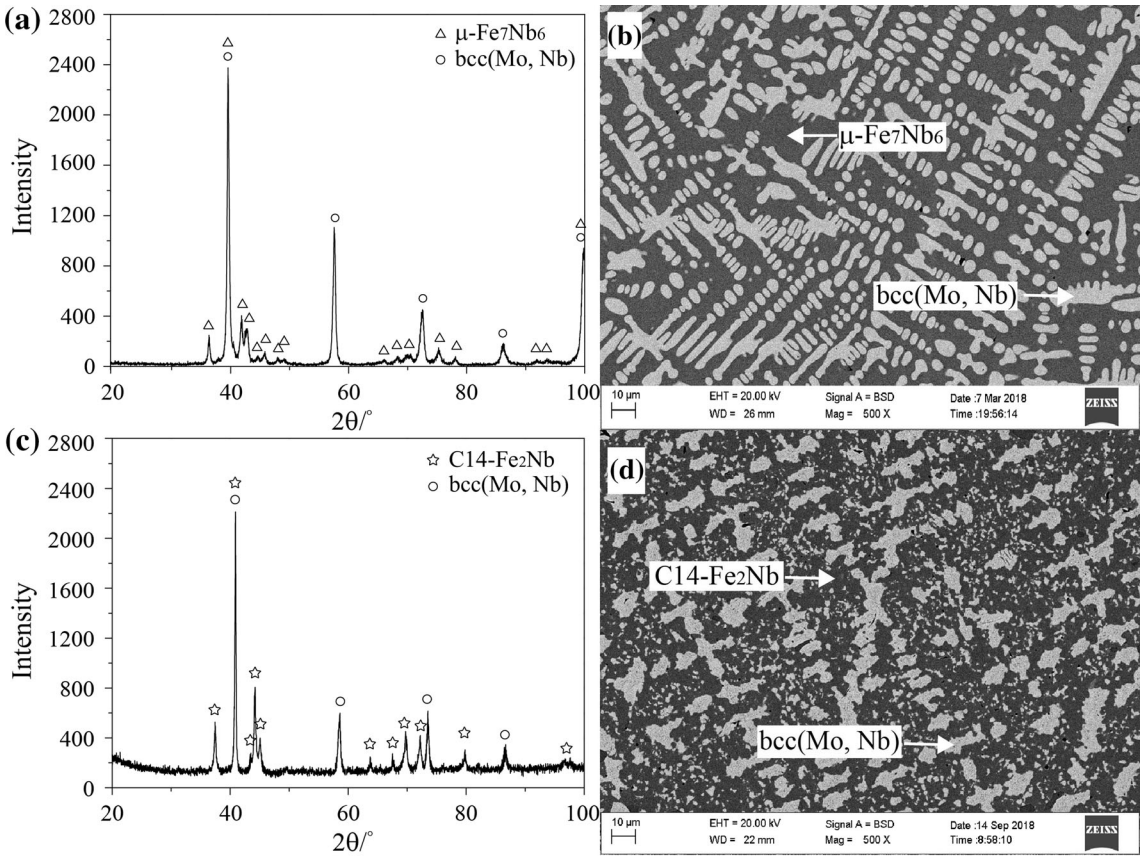

Fig. 7—As-cast alloy #18: (*a*) XRD pattern, (*b*) BSE micrograph, alloy #18 annealed at 1100 °C, (*c*) XRD pattern, (*d*) BSE micrograph.

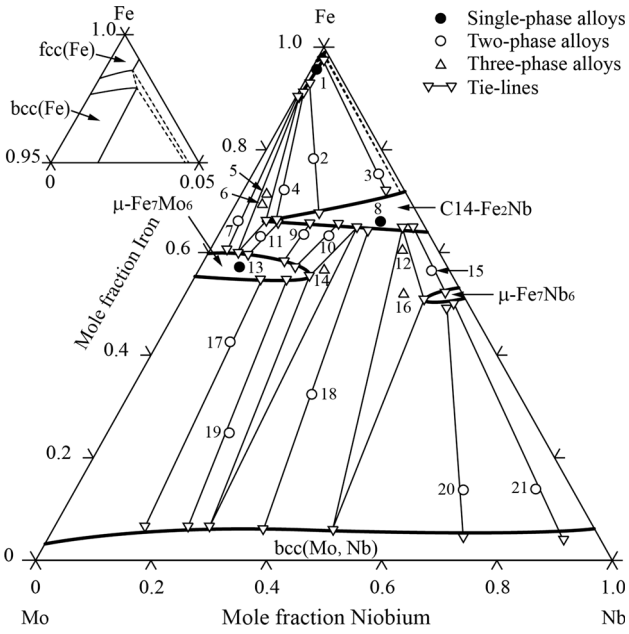

Fig. 8—Isothermal section of the Fe-Mo-Nb system at 1100 °C.

it can be observed that a three-phase microstructure C14-Fe_2Nb + μ-Fe_7Nb_6 + bcc(Mo, Nb) occurred in alloy #16, in agreement with the XRD pattern. Based on the EDS results, the maximum solubility of Mo in μ-Fe_7Nb_6 was determined to be about 10.40 at. pct at 1200 °C.

Based on these experimental results, the isothermal section of the Fe-Mo-Nb system at 1200 °C can be constructed, as presented in Figure 12. The isothermal section at 1200 °C contains six single-phase regions: fcc(Fe), bcc(Fe), bcc(Mo, Nb), C14-Fe_2Nb, μ-Fe_7Mo_6, and μ-Fe_7Nb_6, and three three-phase regions: bcc(Fe) + C14-Fe_2Nb + μ-Fe_7Mo_6, C14-Fe_2Nb + μ-Fe_7Mo_6 + bcc(Mo, Nb), and C14-Fe_2Nb + μ-Fe_7Nb_6 + bcc(Mo, Nb). The solubilities of the C14-Fe_2Nb, μ-Fe_7Mo_6, and μ-Fe_7Nb_6 were measured at 1200 °C.

Mo and Nb are adjacent elements in the elements periodic table, and the C14 crystal structure can flexibly accommodate a third element.[44,45] Thus, large solubilities were measured for Mo in C14-Fe_2Nb in this experimental work.

We also point out that no ternary compounds were found at 1100 °C or 1200 °C.

Table III. Summary of Experimental Results of the Fe-Mo-Nb Alloys Annealed at 1200 °C

	Measured Composition, Atomic Percent				Phase composition, Atomic Percent		
No.	Fe	Mo	Nb	Equilibrium Phase	Fe	Mo	Nb
#1	91.30	7.79	0.91	bcc(Fe)	90.25	8.13	1.62
#2	84.01	8.88	7.11	bcc(Fe)	92.98	5.55	1.47
				C14-Fe_2Nb	67.13	16.05	16.82
#3	80.44	15.09	4.47	bcc(Fe)	89.39	9.88	0.73
				C14-Fe_2Nb	66.20	23.09	10.71
#4	80.42	3.25	16.33	bcc(Fe)	97.56	1.17	1.27
				C14-Fe_2Nb	71.09	5.14	23.77
#5	71.51	25.72	2.77	bcc(Fe)	88.39	10.92	0.69
				μ-Fe_7Mo_6	62.25	34.40	3.35
#6	68.56	24.78	6.66	bcc(Fe)	87.81	11.17	1.02
				C14-Fe_2Nb	65.05	25.51	9.44
				μ-Fe_7Mo_6	61.08	32.38	6.54
#7	65.56	27.07	7.37	bcc(Fe)	88.34	10.12	1.54
				C14-Fe_2Nb	65.48	24.67	9.85
				μ-Fe_7Mo_6	60.26	32.45	7.29
#8	66.95	5.06	27.99	C14-Fe_2Nb	67.57	4.84	27.59
#9	65.91	18.62	15.47	C14-Fe_2Nb	66.63	17.82	15.55
#10	62.50	17.21	20.29	C14-Fe_2Nb	64.62	15.30	20.08
				μ-Fe_7Mo_6	56.56	23.79	19.65
#11	61.74	21.75	16.51	C14-Fe_2Nb	65.00	18.10	16.90
				μ-Fe_7Mo_6	58.21	26.15	15.64
#12	58.66	12.09	29.25	C14-Fe_2Nb	64.48	7.59	27.93
				bcc(Mo,Nb)	6.82	55.99	37.19
#13	57.86	4.21	37.93	C14-Fe_2Nb	63.00	2.77	34.23
				μ-Fe_7Nb_6	51.93	7.71	40.36
#14	52.86	21.18	25.96	C14-Fe_2Nb	63.90	9.77	26.33
				μ-Fe_7Mo_6	54.77	21.38	23.85
				bcc(Mo,Nb)	7.20	63.65	29.15
#15	50.05	31.31	18.64	μ-Fe_7Mo_6	54.02	28.14	17.84
				bcc(Mo,Nb)	6.44	73.50	20.06
#16	45.16	15.30	39.54	C14-Fe_2Nb	63.06	4.70	32.24
				μ-Fe_7Nb_6	50.79	10.40	38.81
				bcc(Mo,Nb)	5.79	43.08	51.13
#17	44.92	19.16	35.92	C14-Fe_2Nb	64.31	4.88	30.81
				bcc(Mo,Nb)	7.47	48.04	44.49
#18	44.39	46.05	9.56	μ-Fe_7Mo_6	55.15	36.06	8.79
				bcc(Mo,Nb)	6.68	83.14	10.18
#19	44.39	8.66	46.95	μ-Fe_7Nb_6	50.39	6.98	42.63
				bcc(Mo,Nb)	5.96	30.67	63.37
#20	9.47	20.62	69.91	μ-Fe_7Nb_6	50.01	4.20	45.79
				bcc(Mo,Nb)	3.95	23.43	72.62

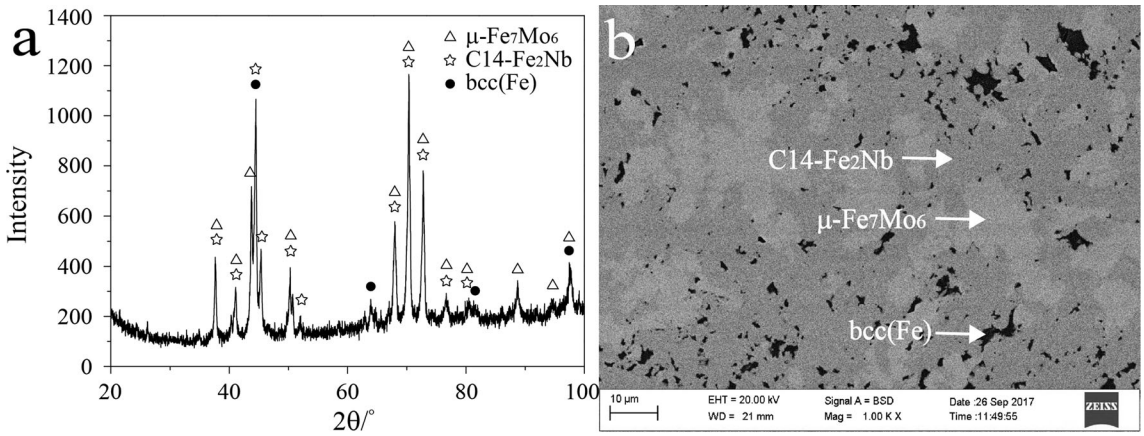

Fig. 9—Alloy #7 annealed at 1200 °C: (*a*) XRD pattern; (*b*) BSE micrograph.

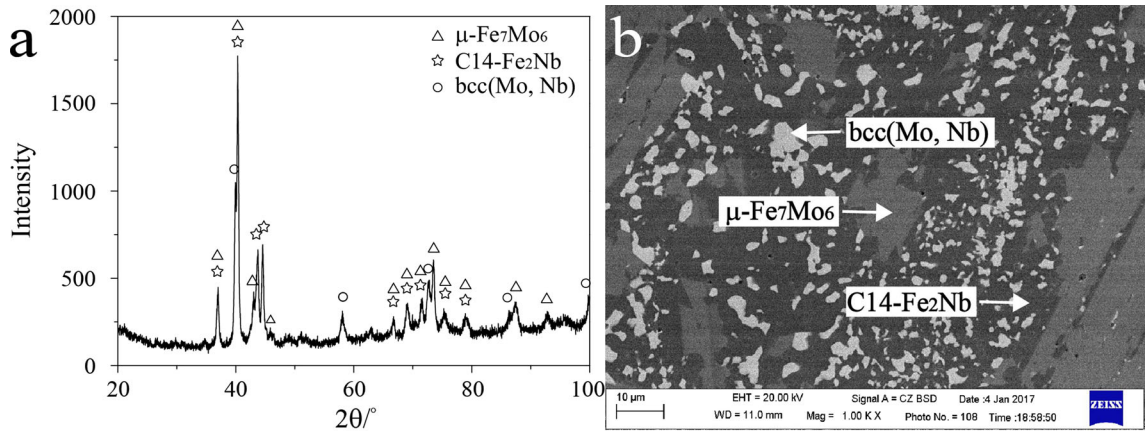

Fig. 10—Alloy #14 annealed at 1200 °C: (*a*) XRD pattern; (*b*) BSE micrograph.

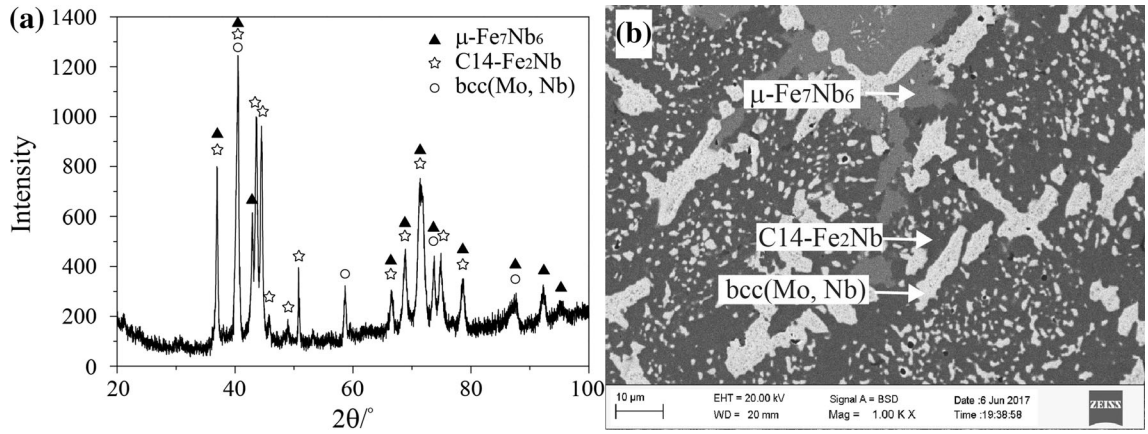

Fig. 11—Alloy #16 annealed at 1200 °C: (*a*) XRD pattern; (*b*) BSE micrograph.

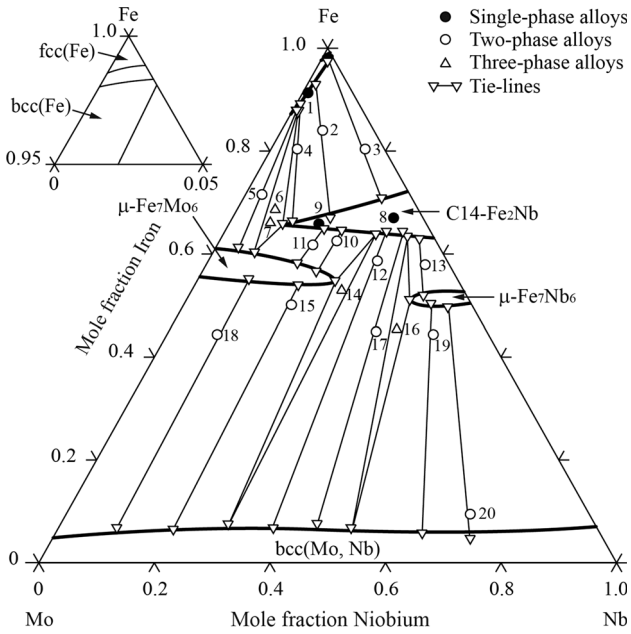

Fig. 12—Isothermal section of the Fe-Mo-Nb system at 1200 °C.

V. CONCLUSIONS

In the present work, the isothermal sections of the Fe-Mo-Nb system were experimentally constructed at 1100 °C and 1200 °C by means of microstructure observation, phase composition measurement, and phase constituent analysis.

The isothermal section of the Fe-Mo-Nb system derived at 1100 °C was found to include four three-phase regions: fcc(Fe) + bcc(Fe) + C14-Fe_2Nb, bcc(Fe) + C14-Fe_2Nb + μ-Fe_7Mo_6, C14-Fe_2Nb + μ-Fe_7Mo_6 + bcc(Mo, Nb), and C14-Fe_2Nb + μ-Fe_7Nb_6 + bcc(Mo, Nb). That at 1200 °C contains three three-phase regions: bcc(Fe) + C14-Fe_2Nb + μ-Fe_7Mo_6, C14-Fe_2Nb + μ-Fe_7Mo_6 + bcc(Mo, Nb), and C14-Fe_2Nb + μ-Fe_7Nb_6 + bcc(Mo, Nb). Ternary compounds were not discovered at 1100 °C or 1200 °C.

The maximum solubility of Mo in C14-Fe_2Nb was determined to be about 26.97 at. pct at 1100 °C, and 25.08 at. pct 1200 °C. Furthermore, C14-Fe_2Mo and C14-Fe_2Nb form a continuous solution, C14-Fe_2(Mo, Nb), in the Fe-Mo-Nb system at 900 °C.[41] Thus, it can be speculated that the solubility of Mo in C14-Fe_2Nb will increase as the temperature decreases until a continuous solution of C14-Fe_2(Mo, Nb) is formed.

The maximum solubilities of Mo in μ-Fe_7Nb_6, and Nb in μ-Fe_7Mo_6 were determined to be about 7.35 and 19.74 at. pct at 1100 °C, respectively. The corresponding values at 1200 °C were measured to be about 10.40 and 23.85 at. pct, respectively.

ACKNOWLEDGMENTS

The work was supported by the National Key R&D Program of China (Grant No. 2016YFB0700501) and National Natural Science Foundation of China (NSFC) (Grant No. 51671025).

REFERENCES

1. S. Jiang, H. Wang, Y. Wu, X. Liu, H. Chen, M. Yao, B. Gault, D. Ponge, D. Raabe, A. Hirata, M. Chen, Y. Wang, and Z. Lu: *Nature*, 2017, vol. 544, pp. 460–64.
2. S. Shanmugam, N.K. Ramisetti, R.D.K. Misra, J. Hartmann, and S.G. Jansto: *Mater. Sci. Eng. A*, 2008, vol. 478, pp. 26–37.
3. V. Knezevic, G. Sauthoff, J. Vilk, G. Inden, A. Schneider, R. Agamennone, W. Blum, Y. Wang, A. Scholz, C. Berger, J. Ehlers, and L. Singheiser: *ISIJ Int*., 2002, vol. 42, pp. 1505–14.
4. L. Falat, A. Schneider, G. Sauthoff, and G. Frommeyer: *Intermetallics*, 2005, vol. 13, pp. 1256–62.
5. Y. Yamamoto, M. Takeyama, Z.P. Lu, C.T. Liu, N.D. Evans, P.J. Maziasz, and M.P. Brady: *Intermetallics*, 2008, vol. 16 (3), pp. 453–62.
6. J.D. Bolton and A.J. Gant: *Powder Metall*., 1996, vol. 39, pp. 27–35.
7. J.D. Bolton and A.J. Gant: *J. Mater. Sci*., 1998, vol. 33, pp. 939–53.
8. S.G. Huang, J. Vleugels, H. Mohrbacher, and M. Woydt: *Int. J. Refrac. Met. Hard Mater*., 2017, vol. 66, pp. 188–97.
9. P.B. Kemp and R.M. German: *Metall. Mater. Trans. A*, 1995, vol. 26A, pp. 2187–89.
10. C.S. Hsu, K.H. Lin, and S.T. Lin: *Int. J. Refrac. Met. Hard Mater*., 2005, vol. 23, pp. 175–82.
11. J. Houserová, J. Vřešťál, and M. Šob: *Calphad*, 2005, vol. 29, pp. 133–39.
12. W.P. Sykes: *Trans. ASST*., 1926, vol. 10, pp. 839–71.
13. W.P. Sykes: *Trans. ASST*, 1929, vol. 16, pp. 358–69.
14. J.L. Ham and D. Mich: *Trans. Am. Soc. Mech. Eng*., 1951, vol. 73, pp. 723–32.
15. W.S. Gibson, J.R. Lee, and W. Hume-Rothery: *J. Iron Steel Inst*., 1961, vol. 198, pp. 64–66.
16. A.K. Sinha, R.A. Buckley, and W. Hume-Rothery: *J. Iron Steel Inst*., 1967, vol. 205, pp. 191–95.
17. J.P. Pivot, A.V. Craeynest, and D. Calais: *J. Nucl. Mater*., 1969, vol. 31, pp. 342–44.
18. C.P. Heijwegen and G.D. Rieck: *J. Less-Common Met*., 1974, vol. 37, pp. 115–21.
19. Y. Ueshima, E. Ichise, and T. Mori: *J. Iron Steel Inst*., 1979, vol. 65, p. S684.
20. E. Ichise, T. Maruo, H. Sasho, Y. Ueshima, and T. Mori: *J. Iron Steel Inst*., 1980, vol. 66, pp. 1075–83.
21. L. Brewer and R.H. Lamoreaux: *At. Energy Rev. II*, 1980, vol. 7, pp. 244–49.
22. T. Takayama, M.Y. Wey, and T. Nishizawa: *Trans. Jpn. Inst. Met*., 1981, vol. 22, pp. 315–25.
23. A.F. Guillermet: *Bull. Alloy Phase Diagr*., 1982, vol. 3, pp. 359–67.
24. P. Gustafson: *Z. Metall*., 1988, vol. 79, pp. 388–96.
25. V.B. Rajkumar and K.C.H. Kumar: *J. Alloys Compd*., 2014, vol. 611, pp. 303–12.
26. N.M. Voronov: *Izv. Akad. Nauk. SSSR Khim*., 1937, vol. 1, pp. 1369–1379.
27. H. Eggers and W. Peter: *Mitt. Kaiser-Wilhelm Inst. Eisenforsch*., 1938, vol. 20, pp. 199–203.
28. R. Genders: *J. Iron Steel Inst*., 1939, vol. 140, pp. 29–37.
29. A. Raman: *Proc. Indian Acad. Sci. A*, 1967, vol. 65, pp. 256–64.
30. W.A. Fischer, K. Lorenz, H. Fabritius, and D. Schlegel: *Arch. Eisenhuttenwes*., 1970, vol. 41, pp. 489–98.
31. H.J. Goldschmidt: *J. Iron Steel Inst*., 1960, vol. 194, pp. 169–80.
32. F.X. Lu and K.H. Jack: *J. Less-Common Met*., 1985, vol. 114, pp. 123–27.
33. B. Zelaya, S. Gama, C.A. Ribeiro, and G. Effenberg: *Z. Metall*., 1993, vol. 84, pp. 160–64.
34. M. Takeyama, N. Gomi, S. Morita, and T. Matsuo: *Mater. Res. Soc. Symp. Proc*., 2005, vol. 842, pp. 461–66.
35. S.K. Balam and A. Paul: *Metall. Mater. Trans. A*, 2010, vol. 41A, pp. 2175–79.
36. S. Voß, M. Palm, F. Stein, and D. Raabe: *J. Phase Equilib. Diffus*., 2011, vol. 32, pp. 97–104.
37. A. Jacob, C. Schmetterer, A. Khvan, A. Kondrtiev, D. Ivanov, and B. Hallstedt: *Calphad*, 2016, vol. 54, pp. 1–15.
38. E. Rudy, C.E. Brukl, and S. Windisch: *Trans. Metall. Soc. AIME*, 1967, vol. 239, pp. 1796–1808.
39. Y.A. Kocherzhinskij and V.I. Vasilenko: *Dokl. Akad. Nauk SSSR*., 1981, vol. 257, pp. 371–73.
40. W. Xiong, Y. Du, Y. Liu, B.Y. Huang, H.H. Xu, H.L. Chen, and Z. Pan: *Calphad*, 2004, vol. 28, pp. 133–40.
41. S.V. Smirnova, L.L. Meshkov, and O.N. Kosolapova: *Moscow Univ. Chem. Bull*., 1987, vol. 42, pp. 84–87.
42. K.C. Harikumar and V. Raghavan: *J. Alloy Phase Diagr*., 1989, vol. 5, pp. 77–96.
43. P. Villars, A. Prince, and H. Okamoto: *Handbook of Ternary Alloy Phase Diagrams*, ASM International, Materials Park, OH, 1995, pp. 10458–64.
44. O. Prymak and F. Stein: *J. Alloy. Compd*., 2012, vol. 513, pp. 378–86.
45. F. Stein: *Mater. Res. Soc. Symp. Proc*., 2011, vol. 1295, pp. 299–310.